



Application of fractal theory and fuzzy enhancement in ultrasound image segmentation

Zhemín Zhuang¹ · Naihai Lei¹ · Alex Noel Joseph Raj¹ · Shunmin Qiu²

Received: 4 April 2018 / Accepted: 26 September 2018
© International Federation for Medical and Biological Engineering 2018

Abstract

The manuscript describes an ultrasound image segmentation technique based on the fractional Brownian motion (FBM) model. Here, the ultrasound images are first enhanced using a fuzzy-based technique, and later the FBM model is employed to obtain the fractal features used for segmentation. The novelty lies in combining the fuzzy-enhancement technique and FBM model, and further illustrating that fractal length-based segmentation provides better results than fractal dimension-based segmentation. Experimental results on ultrasound images of carotid artery clearly illustrate that the segmentation outputs obtained from fractal length are superior, and the high qualitative values of DSC, Precision, Recall and F_1 score (0.9617, 0.9629, 0.9653 and 0.9641 respectively), together with a low value of APD (1.9316), indicate that the proposed method is comparable to other state-of-the-art segmentation techniques.

Keywords Fuzzy enhancement · Fractional Brownian motion (FBM) · Hurst · Fractal dimension · Fractal length · Segmentation

1 Introduction

Computer-aided diagnosis (CAD) employs image processing techniques on medical images to assist doctors in finding lesions and making accurate diagnosis [1, 2]. Ultrasonic diagnosis applies high-frequency sound (ultrasonic) waves to produce images of structures within the human body in order to provide indications of the disease by measuring the morphology of physical structure. It has the advantages of being non-invasive, portable, and inexpensive with real-time dynamic observation and repeated inspection. Hence, ultrasound imaging is often used for identifying cardiovascular disease, abdominal visceral diseases, and superficial organ inspection. Ultrasound image segmentation is very important in CAD, since it acts as the foundation for diagnosis and treatment, premise of quantitative analysis, and three-dimensional reconstruction in clinical practice [3].

The ultrasound images are prone to speckle noise, image artifact, and weak boundaries [4]; therefore, conventional image segmentation methods cannot provide the desired result. Further applying manual segmentation takes time and is prone to subjective errors. In recent decades, many semi-automatic methods for ultrasound image segmentation have been proposed by many researchers. Moursi et al. [5] employed a semi-automatic snake for the segmentation of the carotid artery in ultrasound images. The algorithm requires the user to place a seed point inside the region of interest (ROI), and a rule-based scheme finds the initial contour of the lumen. Later, by carefully adjusting the energies, the contour is refined by the snake scheme. Hossain et al. [6] employed a semi-automatic algorithm to segment the carotid lumen. The algorithm required manual initialization of the contour for the first stage of the segmentation, and later used a distance-regularized level set evolution technique which employed a novel initialization and stopping criteria to locate the lumen–intima boundary (LIB). Automatic segmentation methods use active contours to segment carotid arteries in ultrasound images. Loizou et al. [7–9] improved the snakes algorithm for segmentation of carotid artery in ultrasound images by presenting a complete automated model. The algorithm processed images of the carotid artery with plaques, and measured the intima-media thickness (IMT) of the carotid artery. Molinari et al. [10] proposed a dual-snake system with two different active contours. Here

✉ Alex Noel Joseph Raj
jalxnoel@stu.edu.cn

¹ Department of Electronic Engineering, Shantou University, Shantou, Guangdong, China

² Imaging Department, First Hospital of Medical College of Shantou University, Shantou, Guangdong, China

for automatic segmentation, the parameters α , β , γ are required to be fine-tuned. The algorithm considers both edge strength and shape but needs careful selection of parameters to provide good segmentation results. A local statistics based technique was proposed by Sifakis et al. [11] where the local mean and variance was used to locate the vertical intensity distribution (VIP) of the image and locate the centre point of the lumen. Later, the centre point is refined to accurately estimate the position of the carotid artery. The method is simple and computationally inexpensive, but is sensitive to noise and artifacts [12]. Therefore, the method has usually been used for coarse segmentation that requires further refinement. Supervised learning techniques were also used for ultrasound image segmentation. Qian et al. [13] proposed an integrated learning-based method to segment atherosclerotic carotid plaque which was helpful in the measurement of carotid plaque in ultrasound images. The method permits coarse to fine segmentation through careful selection of ROIs of the ultrasound images. Like any supervised technique, the method requires more training data, with the accuracy depending on the size and the selection of the feature vectors.

Fractal theory is a new discipline in the field of nonlinear mathematics. The main features are self-similarity with fine or detailed structures at an arbitrarily small scale. For fractal theory, the fractal dimension and fractal length are the important parameters that describe the image texture features. At present, fractal theory is employed widely in image processing and medical diagnosis. Omiotek [14] proposed the diagnosis of thyroid gland using fractal theory for ultrasound images. Wang et al. [15] proposed a smoke segmentation method based on the fractional Brownian motion (FBM) model and region growing technique (RGT) to detect smoke in forest-fire images. The method calculated the Hurst parameter, which was used to obtain the binary image. Later, using RGT, the binary images were segmented. The method provided reliable segmentation results for further image analysis and target recognition but required proper selection of Hurst value (threshold value) to obtain binary image. Lin et al. (2013) [16] employed the FBM model for automatic classification of solitary pulmonary nodule in CT images. The fractal feature of the CT image calculated by the FBM model was provided as an input to a trained SVM classifier to determine whether the lung nodule was malignant or not. Lin et al. (2015) [17] proposed a threshold segmentation method for a alveolar bone-loss area localization (ABLIfBm) model that combined intensity and the Hurst value obtained from the FBM model. Here, the leave-one-out cross-validation, training, and testing mechanisms were adopted; ABLIfBm trains weights for both features using Bayesian classifier and transforms the radiograph image into a feature image. Later, using Otsu's thresholding technique, the feature images are segmented into normal regions and bone-loss regions.

The paper proposes a new technique that combines fuzzy enhancement and the FBM model to segment the ultrasound images. Initially, the images are enhanced using a fuzzy-enhancement algorithm described in [18]. Later, the fractal feature of the enhanced ultrasound image is calculated using the FBM model. Here, we propose that features determined using fractal length provide better segmentation results when compared to those obtained from fractal dimension of the ultrasound images of the carotid artery, gallbladder, and liver. Figure 1 compares the segmentation results computed from fractal dimension and fractal length. It is evident that segmentation using fractal length (Fig. 1c) shows a distinct boundary for these images. The paper is organized as follows. Section 2 introduces the fuzzy-enhancement algorithm and the FBM model, followed by section 3 where the results of ultrasound image segmentation are illustrated. The discussion on the segmentation results, followed by the conclusion, are summarized in section 4 and 5 respectively.

2 Methods

The flow diagram of the segmentation process employed in this paper is illustrated in Fig. 2. The ultrasound images are enhanced using the enhancement algorithm explained in [19]. Later, the coarse contours required for segmentation are obtained from the fractal features computed from both fractal dimension and fractal length of the FBM model. These contours are finally refined using morphological operators to get the segmented outputs.

2.1 Fuzzy enhancement and fractional Brownian motion

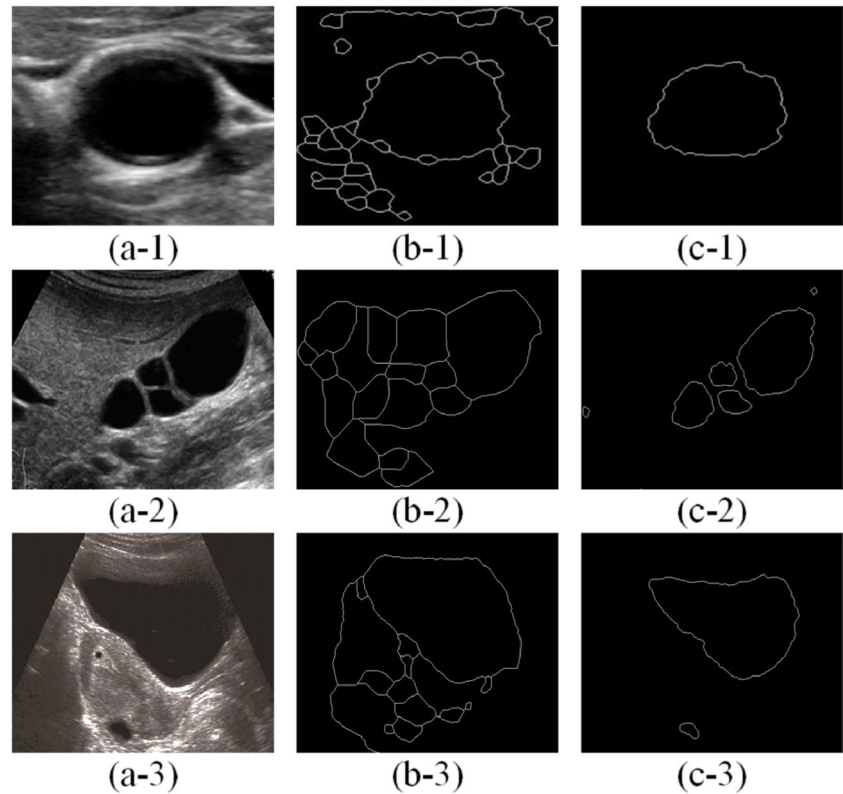
The need for ultrasound image enhancement is to improve the visual effect and highlight the region of interest. Ultrasound images are generally affected by various imaging factors that provide blurry and low-resolution images, which make the segmentation process a difficult task. Further, the gray-scale nature of images is challenging for the human visual system to distinguish the boundaries within images. The fuzziness involved in these images cannot be solved by the classical mathematical theory and thus demands a better way [20, 21]. Therefore a fuzzy-based enhancement technique [19] has been employed.

By using the fuzzy set theory, the pixels in the spatial domain are mapped to their respective fuzzy fields using the membership function defined by Pal [19], as explained in Eq. (1)

$$\mu_{ij} = F(X_{ij}) = [1 + (X_{\max} - X_{ij}) / F_d]^{-F_e} \quad (1)$$

where X_{\max} denotes the maximum gray level ($L - 1$), F_d and F_e are the reciprocal and exponent fuzzy factors respectively, X_{ij}

Fig. 1 Segmentation results. **a** Original image. **b** Using fractal dimension. **c** Using fractal length



is intensity of the pixel at location (i, j) and $\mu_{ij} (\mu_{ij} \in [0, 1])$ is the membership function. Normally F_e is equal to 2 [18] and F_d is experimentally determined. The relationship between the membership function and the gray levels is shown in Fig. 3; here, $L = 256$, $F_e = 2$, and $F_d = 118$.

Therefore according to (1) an image of size $M \times N$ can be repressed as a fuzzy pixels set, P of size $M \times N$ as:

$$P = \begin{bmatrix} \mu_{11} & \mu_{12} & \cdots & \mu_{1N} \\ \mu_{21} & \mu_{22} & \cdots & \mu_{2N} \\ \vdots & \vdots & \cdots & \vdots \\ \mu_{M1} & \mu_{M2} & \cdots & \mu_{MN} \end{bmatrix} \quad (2)$$

Here, in order to increase image contrast, a nonlinear transformation function is used which is defined as:

$$\mu'_{ij} = E_r(\mu_{ij}) = E_1(E_{r-1}(\mu_{ij})), r = 1, 2, 3, 4, \dots \quad (3)$$

$$(where,) E_1(\mu_{ij}) = \begin{cases} 2\mu_{ij}^2 & 0 \leq \mu_{ij} \leq 0.5 \\ 1 - 2(1 - \mu_{ij})^2 & 0.5 < \mu_{ij} \leq 1 \end{cases}$$

where r denotes the number of enhancement. As r increases, the effect of image enhancement will be more. The enhanced images can be obtained by converting the back to spatial domain using the inverse transformation equation given by

$$X'_{ij} = F^{-1}(\mu'_{ij}) = (L-1) + F_d \left[1 - (\mu'_{ij})^{-F_e-1} \right] \quad (4)$$

where X'_{ij} is the gray-scale intensity of enhanced image pixels.

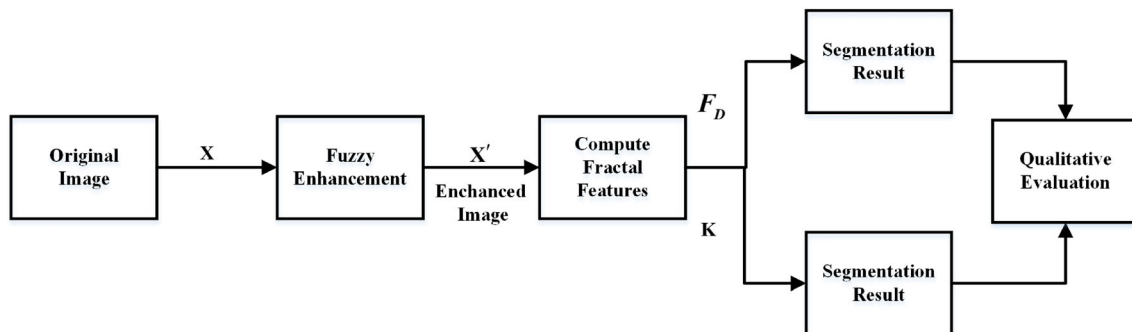


Fig. 2 Flow diagram of the proposed algorithm

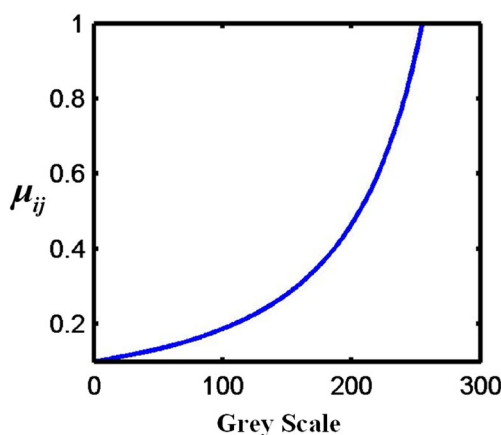


Fig. 3 Membership function curve

In recent years, use of fractal features find applications in medical images, pattern recognition, texture analysis, and image segmentation. Computing the fractal dimension is a vital task in obtaining the fractal features. There are box-counting methods, fractional Brownian motion (FBM) methods and area measurement methods for calculating fractal dimension [22]. Since the FBM model is the most useful and popular model to describe the natural fractal phenomenon [16, 17], here we utilize the FBM model to calculate the fractal features of the image.

In 1923, Wiener proposed a mathematical model that showed randomness similar to Brownian motion, so the Wiener process is also called the random Brownian motion (RBM). RBM is expressed as follows [23].

$$RBM = \begin{cases} B(0) = 0 \\ B(t) \sim N(0, t) \\ E[\Delta B(t)] = 0 \end{cases} \quad (5)$$

(where) $\Delta B(t) = B(t+s) - B(t)$

Mandelbrot and Ness popularized RBM and proposed an FBM model that is used to describe the roughness of the surface. FBM is expressed by Eq. (6) [24, 25].

$$\begin{cases} B_H(0) = b_0 \\ B_H(t) - B_H(0) = \frac{1}{\Gamma(H+0.5)} \int_{-\infty}^t (|t-s|^{H-0.5} - |s|^{H-0.5}) dB(s) \\ + \frac{1}{\Gamma(H+0.5)} \int_0^t |t-s|^{H-0.5} dB(s) \end{cases} \quad (6)$$

where b_0 is a constant. $H(0 < H < 1)$ is the Hurst parameter, $B(s)$ is a RBM function, and $\Gamma(\cdot)$ the gamma function. When $H = 0.5$, $B_H(t) = B(t)$ and FBM is called the general Brownian motion (GBM) model.

The FBM model has the basic characteristics of statistical self-similarity [24], i.e.:

$$B_H(t+hs) - B_H(t) \cong h^H (B_H(t+s) - B_H(t)) \quad (7)$$

where $h > 0$ and \cong infers identical distribution.

From Eq. (7) we can easily obtain the eqs. (8) and (9).

$$E[B_H(t+hs) - B_H(t)] = E[h^H (B_H(t+s) - B_H(t))] \quad (8)$$

$$E[|B_H(t+hs) - B_H(t)|] = h^H E[|B_H(t+s) - B_H(t)|] \quad (9)$$

where E is defined as the expectation. Further by applying the log function to both sides of (9) we obtain

$$\begin{aligned} \log(E[|B_H(t+hs) - B_H(t)|]) &= H \log(h) \\ &+ \log(E[|B_H(t+s) - B_H(t)|]) \end{aligned} \quad (10)$$

Equation (10) follows a linear relationship, $y = Hx + c$, where c is a constant and by using (10), H and c can provide the necessary information for feature computation and image segmentation, which are explained in the following sections.

2.2 Calculation the fractal features of images

To compute the fractal features we employ a sliding-window technique, where the features of the centre pixel of an $n \times n$ window are obtained using the FBM model described in this section. The window is then moved along the horizontal and vertical directions with a step size of l to obtain the fractal features matrix of the whole image. Here, considering computational efficiency and segmentation accuracy, the window size and step length were fixed as 3×3 and 1 respectively.

From eqs. (7) and (10), we can understand that if the incremental $|X(t+\Delta r) - X(t)|$ is stationary, its expectation, $E|X(t+\Delta r) - X(t)|$ is proportional to Δr^H , where Δr represents the distance between the pixels of the $n \times n$ window. Therefore, the relationship between $E|X(t+\Delta r) - X(t)|$ and Δr^H can be expressed as:

$$E|X(t+\Delta r) - X(t)| \propto \Delta r^H \quad (11)$$

From Eq. (11), the distance between Δr and the expectation of difference of any two pixels in the $n \times n$ window can be expressed as in [16]:

$$E(|X(x_2, y_2) - X(x_1, y_1)|) \propto \left(\sqrt{(x_2 - x_1)^2 + (y_2 - y_1)^2} \right)^H \quad (12)$$

By defining $\Delta X_{\Delta r} = X(x_2, y_2) - X(x_1, y_1)$, $\Delta r = \sqrt{(x_2 - x_1)^2 + (y_2 - y_1)^2}$, Eq. (12) reduces to

$$E(|\Delta X_{\Delta r}|) \propto (\Delta r)^H \quad (13)$$

and can be rewritten as

$$E(|\Delta X_{\Delta r}|) = k(\Delta r)^H \quad (14)$$

Further by applying the log function to both sides of (14) we obtain

$$\log(E(|\Delta X_{\Delta r}|)) = H \log(\Delta r) + K \quad (15)$$

where H ($0 < H < 1$) is called the Hurst parameter and K is called fractal length.

On comparing with Eq. (10), $K = \log(E(|\Delta X_{\Delta r}|))$, when $\Delta r = 1$.

From [22, 26] the fractal dimension (F_D) and the Hurst parameter (H) satisfy the following relationship:

$$F_D = 3 - H \quad (16)$$

To determine the fractal dimension: (i) compute H and K value from Eq. (15) by fitting the least-squares linear fit between $\log(E(|\Delta X_{\Delta r}|))$ and $\log(\Delta r)$ as shown in Fig. 4 (here, slope and the intercept provide H and K values respectively), and (ii) substitute H in (16) to obtain F_D .

2.3 Compare fractal dimension and fractal length

In this section, we compare the segmentation results obtained from F_D and K , and illustrate that segmentation results from K are superior to F_D . The fractal dimension represents the change in pixel intensity with respect to pixel distance, and therefore describes the complexity of the texture features within the window. A large value of F_D represents rough texture, and a small value characterizes the smooth texture. On the other hand, K denotes the expectation of the change in pixel intensity between the adjacent pixels of a window, and thus directly relates to the edge features of the image. Both F_D and K can be calculated from Eq. (15) and (16) as explained in the previous section, but the use of K for segmentation would intuitively provide better edges than H . Therefore, we emphasize that image segmentation using K would provide better segmentation results. Figure 5 illustrates the

segmentation results between F_D and K for some of the popular images.

It can be seen that the segmentation results obtained from F_D are prone to noise, with poor visibility of the edges, whereas the segmentation results of K present clear edges with less noise. A detailed comparison of segmentation results between the segmentation based on fractal dimension and segmentation-based fractal length are shown for four different images; this illustrates that the proposed method based on fractal length provides better results than the other techniques. It can be also seen that the window size does not affect the segmentation results, but will affect the computational efficiency of the algorithm; hence, the window size was fixed as 3×3 .

3 Results

The segmentation experiments were performed on ultrasound images of the carotid artery, using MATLAB R2014a executing on an Intel(R) Core(TM) i5-2450 M@2.5GHz(four CPUs) with 4GB RAM. The experiment is divided into three parts:-

- 1) Segmentation results without fuzzy enhancement: The fractal features of original ultrasound images are directly computed using Eq. (16), and the segmentation results obtained using F_D , K and Canny operator are shown in Fig. 6.

From the results, it can be seen that all the three methods fail to provide reliable segmentation if directly applied on the ultrasound images, illustrating the need for image enhancement. The results of the Canny operator (Fig. 6b) show discontinuities, and those of F_D (Fig. 6c) are prone to indistinguishable contours. The

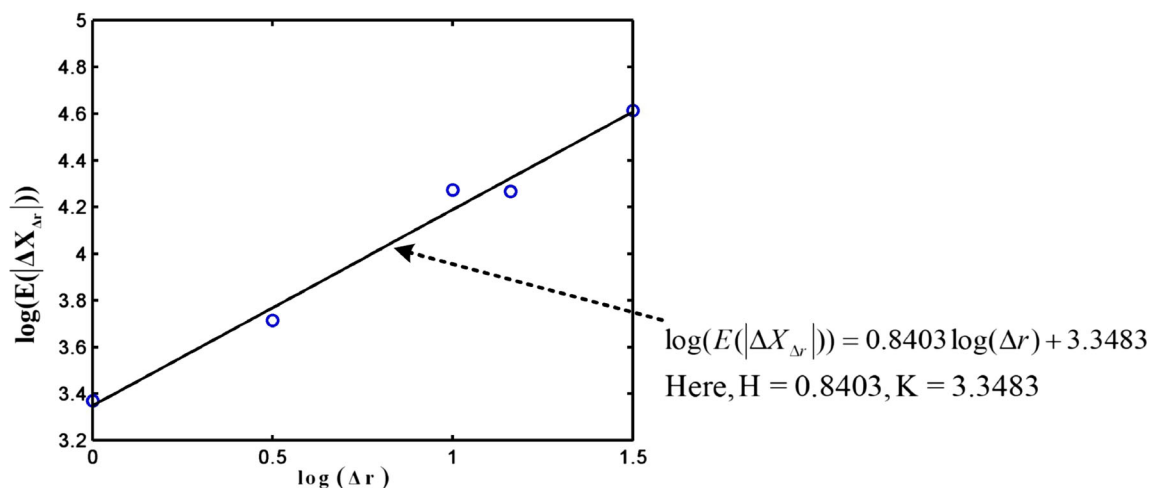
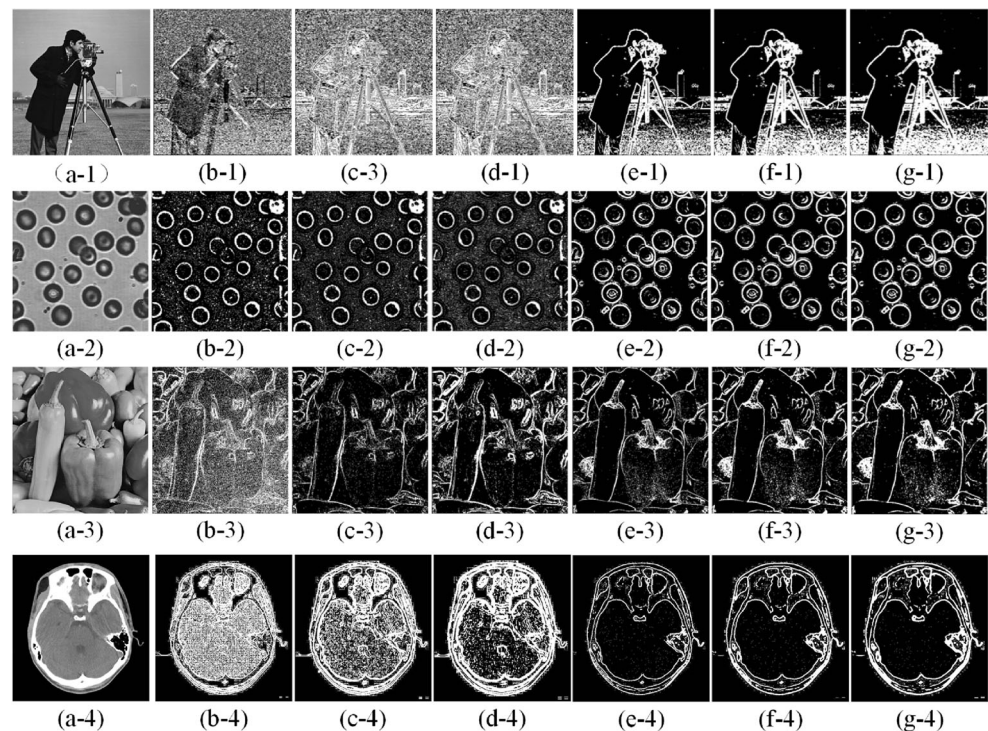


Fig. 4 Computation of H and K — relation between $\log(\Delta r)$ and $\log(E(|\Delta X_{\Delta r}|))$

Fig. 5 Segmentation results of fractal dimension and fractal length with different window sizes. **a** Original image. **b** F_D with 3×3 window. **c** F_D with 5×5 window. **d** F_D with 7×7 window. **e** K with 3×3 window. **f** K with 5×5 window. **g** K with 7×7 window



outputs of K (Fig. 6d), though, clearly show the contour of the bleeding cavity; outputs are prone to noise and poorly segmented regions. This due to the large amount of speckle noise in ultrasound images, which necessitates enhancement to segment the images accurately. The next section illustrates the segmentation results with the fuzzy-enhancement technique explained in section 2.

- 2) Segmentation results with fuzzy enhancement: The ultrasound images are mapped to their fuzzy pixel set using Eq. (1). Here, the values of $F_d = 118$, $F_e = 0.62$, and $r = 5$ were empirically determined. The segmentation results with the enhanced images for all the three operators (Canny, F_D , and K) are shown in Fig. 7:

From the above figures, the original ultrasound image shows poor contrast between the internal and the external

regions of the blood vessels, whereas the enhanced image shows more details, with clear discontinuities with improved visual quality. The Canny operator outputs (Fig. 7c) include a large number of over-segmented regions, whereas for the fractal dimension (Fig. 7d), the contour of the vascular wall is well defined but includes much incorrect segmentation. The results for K (Fig. 7e), although they contain small blobs, have more prominent edges when compared to the other techniques. This illustrates that K-based segmentation is well suited for ultrasound images which suffer from speckle noise, artifact, and poor image quality. The segmentation outputs are later post processed using morphological operations (erosion followed by dilation), and the results are superimposed on the original image as shown in Fig. 8.

From the above figures, it is evident that the segmentation output of K is superior to other segmentation results, since the contours are clear and close to the vascular cavity.

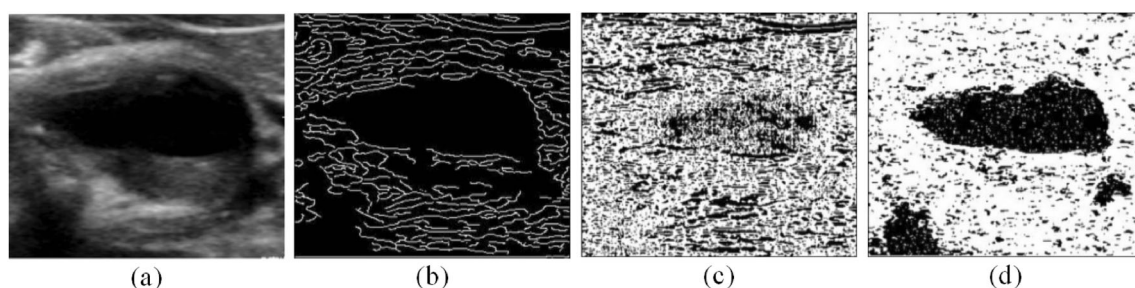


Fig. 6 Segmentation results without fuzzy enhancement. **a** Original image. **b** Segmentation with Canny operator. **c** Segmentation with F_D . **d** Segmentation with K

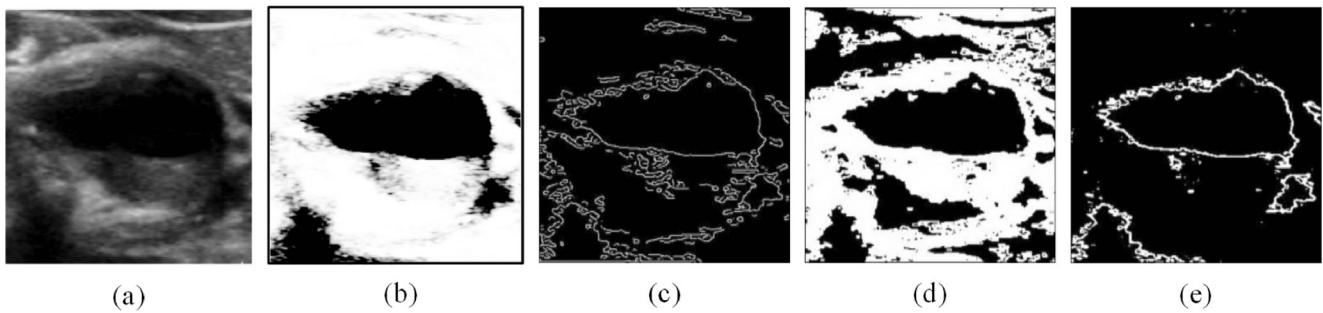


Fig. 7 Segmentation results with fuzzy enhancement. **a** Original image. **b** Enhanced image. **c** Segmentation with Canny operator. **d** Segmentation with F_D . **e** Segmentation with K

- 3) Comparison with other segmentation techniques. The ultrasound images used in our segmentation experiments were provided by the First Affiliated Hospital of Shantou University. Eight ultrasound images of two male cases were considered for our experiments. The first case was diagnosed as bilateral carotid artery stenosis and carotid atherosclerosis, and the second was identified as cerebral infarction of left basal ganglia. The segmentation results obtained by our algorithm were compared with segmentation methods proposed in [27–30].

Li BN et al. [27] combined the spatial fuzzy clustering and the level set method (FCLSM) for automated medical image segmentation. Li C et al. [28] proposed a multiplicative intrinsic component optimization (MICO) for medical image segmentation. Abdelsamea et al. [29] introduced the new active contour models (ACMs) that combined self-organizing map (SOM) and Chan–Vese (C-V) model. Ramamurthy et al. [30] employed a sliding window technique to compute the gray level co-occurrence matrix (GLCM) features, namely Contrast, Correlation, Energy, and Homogeneity along the four directions $[0^\circ, 45^\circ, 90^\circ, 135^\circ]$ of the image for medical image classification. Here, for the ultrasound images of carotid artery, the window size and step length were fixed as 5×5 and 2 respectively. Later, as explained in [30], a K means clustering with $K=2$ was employed to classify the clusters into two classes, namely background and contour of carotid artery. The related code for these algorithms were obtained

from the MATLAB official network. The segmentation results were shown in Fig. 9.

From Fig. 9, it can be seen that the segmentation results of techniques explained in [27–29] and [30], along with the F_D -based segmentation method, do not provide a clear contour of the original image, and contain many undesirable regions when compared with the outputs of K-based segmentation.

4 Discussion

The effectiveness of the segmentation results were quantitatively compared using the following parameters: Dice similarity coefficient (DSC) [31], Precision, Recall, and F_1 score [31] and average perpendicular distance (APD) [32]. These parameters can be computed from the following equations:

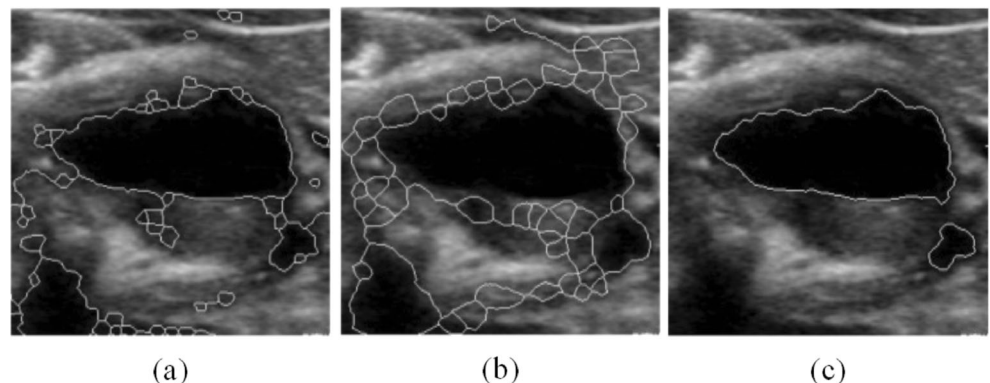
$$DSC = \frac{2|S_{GT} \cap S_S|}{|S_{GT}| + |S_S|} \quad (17)$$

$$Precision = \frac{S_{GT} \cap S_S}{S_{GT}} \quad (18)$$

$$Recall = \frac{S_{GT} \cap S_S}{S_S} \quad (19)$$

where, S_{GT} represents the area of ground truth manually delineated by the doctor, and S_S represents the area of the

Fig. 8 Post-processed segmentation outputs superimposed on the original image (white line: segmentation output post processed by morphological operations). **a** Canny **b** F_D . **c** K



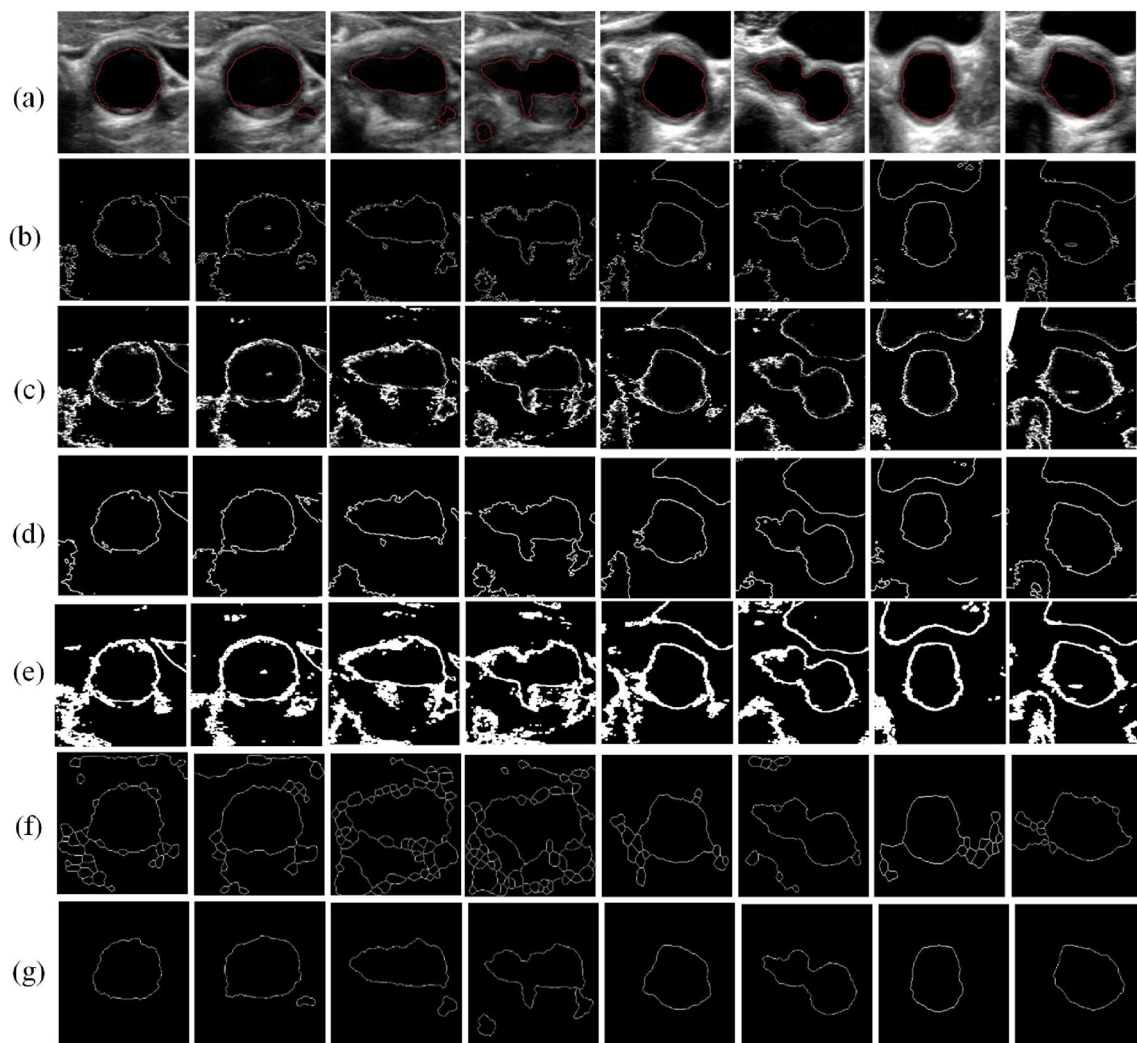


Fig. 9 Comparison with other segmentation techniques. **a** Original image showing the ground truth marked in red **b** Segmentation using the method of Li BN et al. [27]. **c** Segmentation using the method of Li C

et al. [28]. **d** Segmentation using the method of Abdelsamea et al. [29]. **e** Segmentation using the method of Ramamurthy et al. [30]. **f** Segmentation using F_D . **g** Segmentation using K

segmented contour. The F_1 score, defined as the harmonic mean of precision and recall is calculated as

$$F_1 = 2 \times \frac{\text{Precision} \times \text{Recall}}{\text{Precision} + \text{Recall}} \quad (20)$$

The APD, which measures the distance between the automatically segmented contour and its corresponding manually drawn counterpart, is calculated as

$$APD = \frac{1}{n} \sum_{i=1}^n d_i \quad (21)$$

Where d_i is the distance from the segmented contour to the ground truth manually delineated by the doctor.

Table 1 presents the evaluation results of various techniques. These measures were obtained from the enhanced images. The qualitative values obtained from fractal length (K)-based segmentation results have a DSC of 0.9617, and

Precision, Recall, and F_1 scores of 0.9629, 0.9653, and 0.9641 respectively. These high values indicate that the segmentation result is comparable to the ground truth. A low-value APD = 1.9316 illustrates that the contour of the segmented result is close to the contour of ground truth. Moreover, the segmentation results from other techniques have lower values of DSC, Precision, Recall, and F_1 score, and high values of APD. Therefore, these results indicate that the K segmentation is better than F_D and other segmentation techniques.

5 Conclusion

The paper presents a segmentation algorithm that is well suited for ultrasound images which are prone to speckle noise and artefacts. Here, a combination of fuzzy-based-enhancement algorithm, along with fractal-length-based features computed

Table 1 Performance evaluation of various methods

	Li BN [27] (FCLSM)	Li C [28] (MICO)	Abdelsamea [29] (ACMs)	Ramamurthy [30] (GLCM)	Fractal dimension	Fractal length
DSC	0.7173	0.6572	0.7817	0.7258	0.7079	0.9617
Precision	0.5990	0.5017	0.7064	0.5706	0.5643	0.9629
Recall	0.9450	0.9926	0.8863	0.9993	0.9984	0.9653
F_1	0.7332	0.6665	0.7874	0.7264	0.7211	0.9641
APD	32.0774	37.0761	43.7511	40.6432	34.8390	1.9316

from the FBM model, is employed to provide clear contours with less discontinuity. The experimental results, followed by qualitative analysis on ultrasound images of carotid artery, show that the segmentation results obtained from fractal-length-based features are better than other state-of-art techniques.

Acknowledgements This research was financially supported by the Foundation of China (No.61471228), the Key Project of Guangdong Province Science & Technology Plan (No. 2015B020233018), and the Scientific Research Grant of Shantou University, China, Grant No: NTF17016.

References

- Jiang M, Zhang S, Li H, Metaxas D (2015) Computer-aided diagnosis of mammographic masses using scalable image retrieval. *IEEE Trans Biomed Eng* 62(2):783–792
- Moon WK, Shen YW, Huang CS, Chiang LR, Chang RF (2011) Computer-aided diagnosis for the classification of breast masses in automated whole breast ultrasound images. *Ultrasound Med Biol* 37(4):539–548
- Han SM, Lee HJ, Jin YC (2008) Computer-aided prostate cancer detection using texture features and clinical features in ultrasound image. *J Digit Imaging* 21(1):121–133
- Shanmugam N, Suryanarayana AB, Tsb S, Chandrashekar D, Manjunath CN (2011) A novel approach to medical image segmentation. *J Comput Sci* 7(5):657–663
- Moursi SG, Sakka MRE (2009) Semi-automatic snake based segmentation of carotid artery ultrasound images. *Commun Arab Comput Soc (ACS)* 2(2):1–32
- Hossain MM, AlMuhanna K, Zhao L, Lal B, Sikdar S (2015) Semiautomatic segmentation of atherosclerotic carotid artery lumen using 3d ultrasound imaging. *Med Phys* 42(4):2029–2043
- Loizou CP, Nicolaides A, Kyriacou E, Georgiou N, Griffin M, Pattichis CS (2015) A comparison of ultrasound intima-media thickness measurements of the left and right common carotid artery. *IEEE J Translat Eng Health Med* 3:1–10
- Loizou CP, Pattichis CS, Pantziaris M, Tyllis T, Nicolaides A (2007) Snakes-based segmentation of the common carotid artery intima media. *Med Biol Eng Comput* 45(1):35–49
- Loizou CP, Petroudi S, Pantziaris M, Nicolaides AN, Pattichis CS (2014) An integrated system for the segmentation of atherosclerotic carotid plaque ultrasound video. *IEEE Trans Ultrason Ferroelectr Freq Control* 61(1):86–101
- Molinari F, Meiburger KM, Saba L, Acharya UR, Ledda M, Nicolaides A, Suri JS (2012) Constrained snake vs. conventional snake for carotid ultrasound automated IMT measurements on multi-center data sets. *Ultrasonics* 52(7):949–961
- Sifakis EG, Golemati S (2014) Robust carotid artery recognition in longitudinal B-mode ultrasound images. *IEEE Trans Image Process* 23(9):3762–3772
- Meiburger KM, Acharya UR, Molinari F (2018) Automated localization and segmentation techniques for B-mode ultrasound images: a review. *Comput Biol Med* 92:210–235
- Qian C, Yang X (2018) An integrated method for atherosclerotic carotid plaque segmentation in ultrasound image. *Comput Methods Programs Biomed* 153:19–32
- Omiotek Z (2017) Fractal analysis of the grey and binary images in diagnosis of Hashimoto's thyroiditis. *Biocybernet Biomed Eng* 37(4):655–665
- Wang X, Jiang A, Wang Y (2011) A segmentation method of smoke in forest-fire image based on fbm and region growing. In: *Proceedings of Chaos–Fractals Theories and Applications (IWCFTA) 2011: IEEE Fourth International Workshop in Hong Kong, China* (pp. 390–393)
- Lin PL, Huang PW, Lee CH, Wu MT (2013) Automatic classification for solitary pulmonary nodule in CT image by fractal analysis based on fractional Brownian motion model. *Pattern Recogn* 46(12):3279–3287
- Lin PL, Huang PW, Huang PY, Hsu HC (2015) Alveolar bone-loss area localization in periodontitis radiographs based on threshold segmentation with a hybrid feature fused of intensity and the H-value of fractional Brownian motion model. *Comput Methods Prog Biomed* 121(3):117–126
- Hasikin K, Isa NAM (2013) Fuzzy image enhancement for low contrast and non-uniform illumination images. In: *Proceedings of Signal and Image Processing Applications (ICSIPA) 2013: IEEE International Conference, Melaka, Malaysia* (pp. 275–280)
- Wang Y, Li D, Xu Y (2013) An improved image enhancement algorithm based on fuzzy sets. In: *Conference Anthology, China, IEEE* (pp. 1–4)
- Hasikin K, Isa NAM (2012) Enhancement of the low contrast image using fuzzy set theory. In: *Proceedings of UKSim, International Conference on Computer Modelling and Simulation, United Kingdom* (pp. 371–376)
- Binaee K, Hasanzadeh RP (2014) An ultrasound image enhancement method using local gradient based fuzzy similarity. *Biomed Signal Process Contrl* 13:89–101
- Lopes R, Betrouni N (2009) Fractal and multifractal analysis: a review. *Med Image Anal* 13(4):634–649
- Bojdecki T, Gorostiza LG, Talarczyk A (2004) Sub-fractional Brownian motion and its relation to occupation times. *Stat Proba Lett* 69(4):405–419
- Lundahl T, Ohley WJ, Kay SM, Siffert R (1986) Fractional Brownian motion: a maximum likelihood estimator and its application to image texture. *IEEE Trans Med Imaging* 5(3):152–161

25. Boufoussi B, Hajji S (2012) Neutral stochastic functional differential equations driven by a fractional Brownian motion in a Hilbert space. *Stat Proba Lett* 82(8):1549–1558
26. Zachevsky I, Zeevi YY (2014) Single-image superresolution of natural stochastic textures based on fractional Brownian motion. *IEEE Trans Image Process* 23(5):2096–2108
27. Li BN, Chui CK, Chang S, Ong SH (2011) Integrating spatial fuzzy clustering with level set methods for automated medical image segmentation. *Comput Biol Med* 41(1):1–10
28. Li C, Gore JC, Davatzikos C (2014) Multiplicative intrinsic component optimization (MICO) for MRI bias field estimation and tissue segmentation. *Magn Reson Imaging* 32(7):913–923
29. Abdelsamea MM, Gnecco G, Gaber MM (2017) A SOM-based Chan–Vese model for unsupervised image segmentation. *Soft Comput* 21(8):2047–2067
30. Ramamurthy B, Chandran KR (2012) Content based medical image retrieval with texture content using gray level co-occurrence matrix and k-means clustering algorithms. *J Comput Sci* 8(7):1070–1076
31. Gottron, T. (2008). Content code blurring: a new approach to content extraction. In: DEXA '08 Proceedings of the 2008 19th International Conference on Database and Expert Systems Application, Turin, Italy (pp. 29–33). IEEE
32. Ostry DJ, Darainy M, Mattar AA, Wong J, Gribble PL (2010) Somatosensory plasticity and motor learning. *J Neurosci* 30(15): 5384–5393



Zhemin Zhuang Zhemin Zhuang received the B.Eng. degree in Electrical Engineering, the M.S. degree in Precision Instrument, and the Ph.D. degree in Measuring and Testing Technologies and Instruments from Southeast University, in 1986, 1992, and 2002 respectively. Since 2005, he has been a professor with the Department of Electronic Engineering, Shantou University. He has authored or coauthored more than 30 papers published in refereed journals.

His research interests include medical imaging processing and Intelligent signal processing.



Naihai Lei Naihai Lei received the bachelor degree in applied mathematics from Henan University of Technology in 2015. He is now a graduate student at Shantou University, in Department of Electronic Engineering. His research interests include medical imaging processing and Intelligent signal processing.



Alex Noel Joseph Raj Alex Noel Joseph Raj received the B.E. degree in Electrical Engineering from Madras University, India, in 2001, the M.E. degree in Applied Electronics from Anna University in 2005, and the Ph.D. degree in Engineering from the University of Warwick in 2009. From October 2009 to September 2011, he was with Valeport Ltd Totnes, UK as Design Engineer. From March 2013 to March 2017 he was with the Department of

Embedded Technology, School of Electronics Engineering, VIT University, Vellore, India as a Professor. Since March 2017, he is with Department of Electronic Engineering, College of Engineering, Shantou University, China. His research interests include Machine Learning, Signal and Image Processing and FPGA implementations.



Shunmin Qiu Shunmin Qiu received both B.Sc. and M.Sc. degree from Shantou University, China. She used to be an exchange student in Hong Kong Polytechnic University. Now, she is an ultrasound doctor at the First Hospital of Medical College of Shantou University. Her research interests include echocardiography and ultrasound contrast.